Structural modeling of antibody variant epitope specificity with complementary experimental and computational techniques

Eva Smorodina, Puneet Rawat
Dept. of Immunology, University of Oslo & Oslo Univ. Hospital, Norway
{eva.smorodina,puneet.rawat}@medisin.uio.no

Lucas Matthias Weissenborn, Khang Lê Quý, Brij Bhushan Mehta
Dept. of Immunology, University of Oslo & Oslo Univ. Hospital, Norway
{l.m.weissenborn,q.k.le,b.b.mehta}@medisin.uio.no

Oliver Crook
Dept. of Statistics, University of Oxford, UK
oliver.crook@stats.ox.ac.uk

Rahmad Akbar
Antibody Discovery, Novo Nordisk, Denmark
rdak@novonordisk.com

Aleksandar Antanasijevic
School of Life Sciences, EPFL, Switzerland
aleksandar.antanasijevic@epfl.ch

Johannes Loeffler, Hannah Turner, Monica Fernandez-Quintero
Integrative Structural & Comp. Biology, Scripps Res. Inst., USA
{jloeffler,hannaht,mfernandez,andrew}@scripps.edu

Ole Magnus Fløgstad, Dario Segura Pena, Nikolina Sekulic
Centre for Molecular Medicine, EMBL Partnership, Norway
o.m.flogstad@ncmm.uio.no, {d.s.pena,nikolina.sekulic}@biotek.uio.no

Fridtjof Lund-Johansen, Jan Terje Andersen, Victor Greiff
Dept. of Immunology, University of Oslo & Oslo Univ. Hospital, Norway
{fridtjl,j.t.andersen,victor.greiff}@medisin.uio.no

Abstract

Antibodies are key therapeutic biomolecules yet the principles underlying diverse paratopes binding to the same epitope remain unexplained. An insufficient understanding of the structural rules of antibody-antigen binding, due to a lack of experimentally resolved structures, leads to the current inability to characterize antibody variants in silico. Here we explore a rule-based antibody design strategy that relies on a thorough understanding of epitope-paratope interactions, in contrast to generative design based on millions of trials and errors. We identified the epitope of six affinity-verified complexes between HER2 and Trastuzumab paratope variants using cryo-EM and position-resolved HDX-MS. Computational analysis of modeled structural conformational ensembles replicates and expands experimental results and highlights the importance of flexibility in understanding high and low-affinity binders. Structural parameters calculated based on geometry, surface, and biochemical properties were able to stratify antibodies by affinity. Overall, our study describes the structural interfaces of the paratope variants, showing how antibodies with diverse sequences share similar binding rules.

1 Introduction

Antibodies are leading drugs against cancer, infectious, and autoimmune diseases estimated to reach 445 billion USD in market sales by 2028 (Lyu et al., 2022). The biomedical and commercial success of antibodies may be explained by the potential to engineer antibodies specific to nearly any target molecule (antigen). Antibodies consist of four polypeptide chains – two heavy (H) and two light (L) – connected by disulfide bridges (Chiu et al., 2019). The main diversity of antibody sequences is concentrated in complementarity-determining regions (CDRs) located within the variable domains (VH and VL) of the antibody structure (Chiu et al., 2019; Wilson & Stanfield, 2021). Among all CDRs, the CDRH3 is particularly interesting as it is the source of the highest sequence diversity and has been shown previously to play a predominant role in binding (Xu & Davis, 2000; Akbar et al., 2021).

CDRs are flexible and dynamic, providing sufficient plasticity for a conformational complementarity to the antigen binding site (epitope) (Bashour et al., 2024; Guo et al., 2023; Park & Izadi, 2024). Experimental techniques that can capture molecular flexibility (e.g., cryo-EM) are widely used for protein structure determination (Klebe, 2024; Chen et al., 2022). However, high cost and processing time and a low success rate cause the lack of experimentally resolved structures (Hummer et al., 2022), leading to the need for computational approaches to model antibody-antigen binding.

It is known that sequence-similar and sequence-dissimilar antibodies can bind to the same epitope (Mason et al., 2021; Robinson et al., 2021; Wong et al., 2021; Chinery et al., 2024) suggesting an immense binding space of possible antibodies for one epitope. For example, there exist HER2-binding ¿10^5 Trastuzumab variants (Mason et al., 2021; Chinery et al., 2024). While previous studies found that CDRH3 regions can maintain structural similarity despite sequence differences, they left unexplained the fundamental rules – the how and why – behind this structural conservation (Wong et al., 2021). Understanding the structural rules that allow diverse CDRH3 sequences to bind to the same epitope requires careful study of the underlying biological, chemical, and physical principles, along with the forces that drive these interactions.

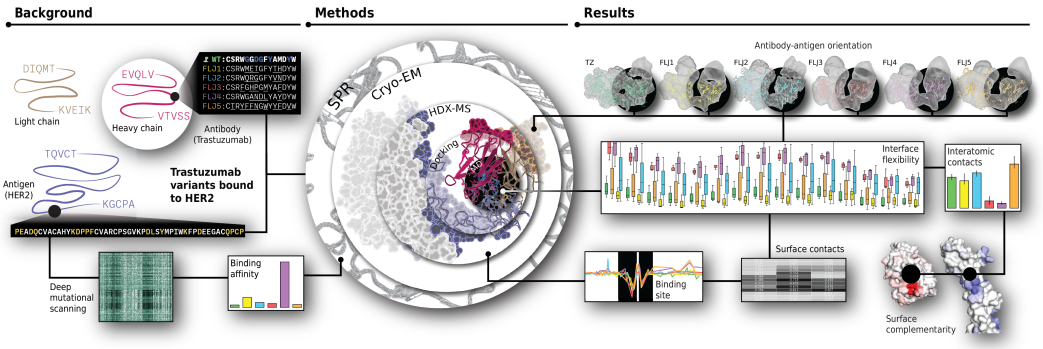

Figure 1: **Antibody-antigen binding consists of different levels of complexity.** The progression from global binding properties to interatomic contacts revealed hidden structural principles underlying antibody variant binding, previously obscured by insufficient refinement.

2 Results

To investigate how different paratope variants bind to the same epitope, we used a model system of six TZ sequences: one WT and five variants (hereafter named FLJ1, FLJ2, FLJ3, FLJ4, and FLJ5) (Figure 1, Table S1). We performed experimental and computational analysis of their structure and binding to HER2. All variants differed from the WT sequence by, on average, 5 amino acids (33%) in the 15 amino acid long CDRH3 region compared to the WT sequence (96-CSRWGGDGFYAMDYW-110, IMGT numbering scheme) (Table S1). All other parts of the complex, including the epitope, remained unmodified, leading to

the same sequence length for all antibody variants and the antigen. With such substantial differences in CDRH3 sequence, we first tested if all TZ variants showed binding to HER2 using surface plasmon resonance (SPR). SPR binding kinetics data of TZ WT and TZ variants with HER2 indicated that all the tested variants and WT antibody have affinities (K_{D}) in the predominantly nanomolar (nM) range. FLJ2 showed the highest affinity (K_{D} = 0.35 nM) and FLJ4 variant showed the lowest affinity (K_{D} = 77.5 nM). The rest of the variants showed K_{D} within a range of 0.72-2.03 nM (Table S1). To conclude, 4 out of 5 TZ variants (all except FLJ4) showed comparably high binding affinity to HER2 as TZ WT.

Next, to identify the binding site of each TZ variant, we performed experimental structure determination using cryogenic electron microscopy (cryo-EM). The high flexibility of the binding interface (Ruedas et al., 2024) had both beneficial and detrimental effects. Specifically, the high flexibility of the epitope resulted in low-resolution cryo-EM maps (Figure S1A, Figure 2A). However, this provided us with the insight that interface dynamics play a crucial role in TZ-HER2 binding and led us to explore the binding flexibility and dynamics in greater detail.

We applied hydrogen-deuterium exchange (HDX) mass spectrometry (MS) (Masson et al., 2019) to experimentally refine the cryo-EM binding interface from the epitope side and gain additional insights into HER2 binding flexibility. HDX-MS measures deuterium uptake in peptides, into which the antigen is divided, highlighting bound regions through lower uptake values. The lowest uptakes are observed at the periphery of the epitope (555-567 and 587-601), while the central region (576) shows higher uptake values, suggesting a nonlinear (conformational) epitope with lower binding strength in the middle (Figure 2B). These results indicate the great structural importance of the epitope conformation in these regions and reveal slight differences in the interactions of the HER2-TZ variants. However, HDX-MS provides only peptide-level resolution, leading to the need for additional computational techniques to obtain the residue-wise results.

First, we applied ReX (Crook et al., 2024), a statistical approach for achieving residue-level uptakes in HDX-MS peptide-level measurements. Residue-wise protection is confirmed identical to the peptide-wise epitope with residues in the span 563-573 and around 593 showing a high probability of protection. Supervised conformational signature analysis (sCSA) in combination with orthogonal partial least squares discriminant analysis (OPLS-DA) concluded that for some residues, HDX variation is not associated with binding affinity (Figure 2D, upper and lower triangle), for some residues, higher flexibility (Figure 2D, higher uptake) is associated with binding affinity and for some lower flexibility (lower uptake) is associated with higher binding affinity. Most residues at 1 and 100 minutes show that decreased uptake correlates with higher binding affinity. No single residue is highly predictive, suggesting many small effects contribute to affinity. At 1 minute, residues at the antibody-antigen interface show decreased uptake, with more flexibility at residues 567 and 568 linked to higher affinity, indicating a subtle conformational change. At 100 minutes, variability increases, with both increased and decreased flexibility in the epitope region being important. Furthermore, the residues where variability is most predictive have changed, suggesting that the epitope region and critical residues are dynamic.

Second, we applied molecular dynamics (MD) simulations to obtain the flexibility data ab initio (independent from HDX-MS) and for both epitope and paratope residues (in contrast to HDX-MS and ReX, which revealed flexibility only of the epitope). We had two groups of initial rigid models as an input for MD simulations: 1) all TZ variants have the same binding orientation as TZ WT (called "FoldX", no docking applied), and 2) the antibody-antigen orientation is adjusted compared to rigid TZ WT (called "ClusPro", docking applied). Then we applied 300 ns classical MD simulations with 3 repetitions for each system. MD revealed high fluctuations of the antigen binding region (Figure 2B), explaining why many experimental structures have missing atoms in the epitope. These fluctuations can be measured quantitatively through root mean squared fluctuations (RMSF) that highlights which regions of a molecule are mobile or rigid, revealing functional dynamics and stability. We computed RMSF over the full MD trajectories for antibody (CDRH3) and antigen (global binding region) independently. Antibody RMSF at the CDRH3 region highlighted residue-wise flexibility differences between variants through time (Figure 2B, left). FLJ4 and FLJ3 show noticeably higher RMSD values for residues 96-108 for ClusPro and FLJ4 for 99-105

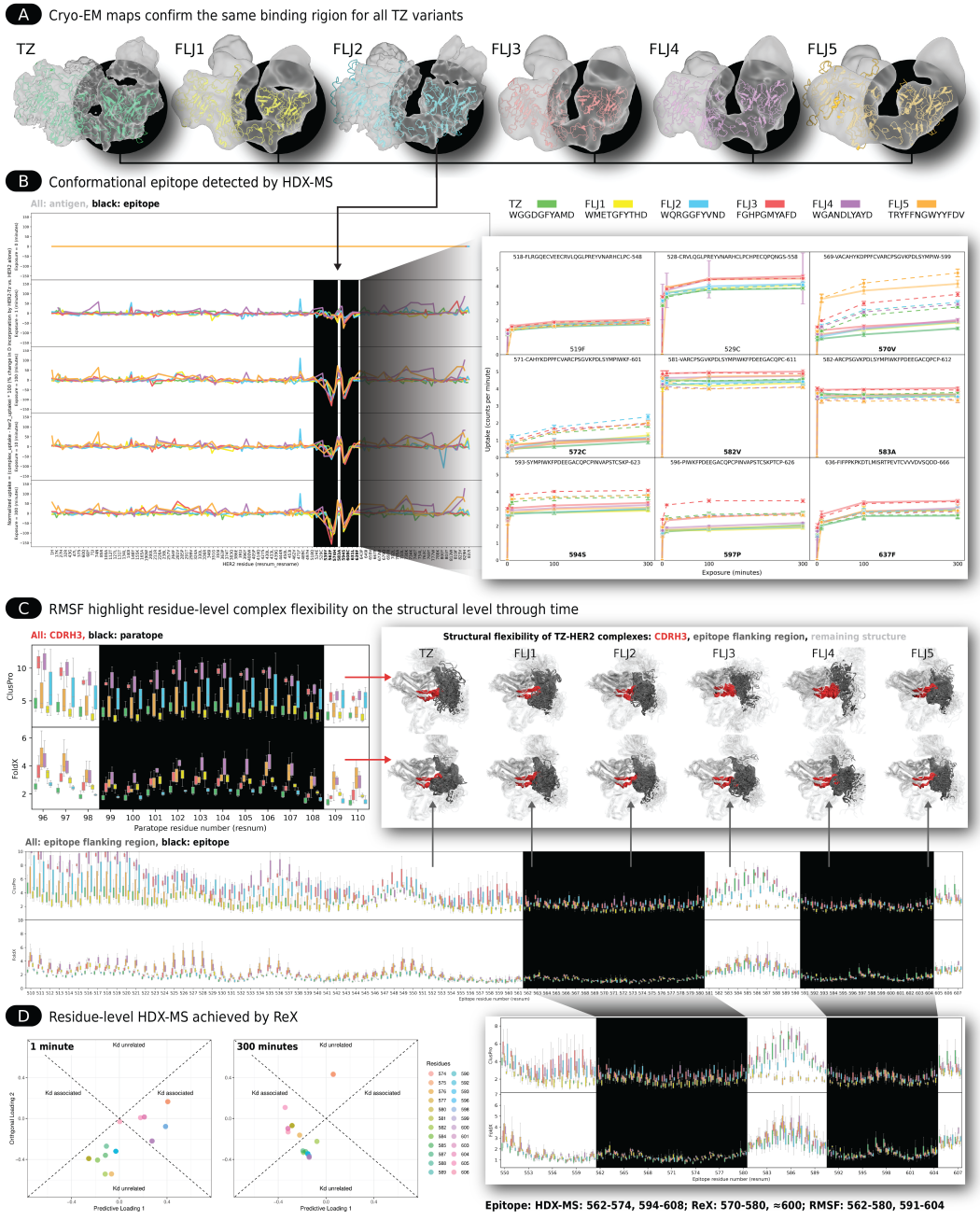

Figure 2: **Tested TZ variants share a position-based HER2 epitope, with flexibility in the binding interface detectable via cryo-EM, HDX-MS, RMSF, and ReX.** Variant colors: TZ WT (green), FLJ1 (yellow), FLJ2 (blue), FLJ3 (red), FLJ4 (purple), FLJ5 (orange). **A.** Cryo-EM maps show all variants bind the same region. Density maps (gray) and FoldX-modeled structures (cartoons) were aligned for optimal fit. FLJ2 and FLJ5 had the poorest fit (79% and 74%), while others averaged 93.75%. Binding region is shown in black. **B.** HDX-MS refined the binding site to peptides spanning residues 555–567 and 587–601. Bound regions (black) showed reduced deuterium uptake, especially at residues 563, 565, 587, and 597. **C.** RMSF aligned with HDX-MS, revealing binding regions (562–580, 591–604) with low fluctuation. FLJ4, the weakest binder, had the highest RMSF. Structural models show RMSF patterns, with CDRH3 in red and epitope in dark gray. **D.** ReX data matched RMSF findings. OPLS-DA plots linked specific residues to SPR Kd: early-time associations include 567–581; later-time include 573–599, with both increased and decreased flexibility linked to affinity.

for FoldX which is in line with SPR experiments that identified FLJ4 as the worst binder (worst K_D and K_{off}) and FLJ3 as the binder with the second worst K_{off}. On the antigen side, when we looked at the RMSF values at the global binding region we found two parts with noticeably lower RMSF values that span over residues 562-580 and 591-604. These regions are aligned with conformational epitope detected by HDX-MS (555-567 and 587-601 + 9 on average amino acids resolution) and ReX (563-573 and around 593) (Figure 2). These findings suggest that RMSF can identify the residues involved in TZ binding to HER2 and among the interacting residues RMSF is higher for weaker binders.

Having confirmed the importance of flexibility in binding, we focused on identifying specific interactions between TZ WT and TZ variants and HER2 to explain their binding. To prove that we can define the correct contacts computationally, we calculated solvent-accessible surface area (SASA). SASA measures residue exposure to solvent, with low values indicating inter- or intra-molecular contacts. To focus only on the binding-induced contact changes, we normalized bound SASA values by unbound values. SASA revealed that residues 100-105 on the paratope and 550-553, 564-567, 576-580, 592-600, and 609-612 on the epitope were significantly lower than others in the binding region, suggesting they play key roles in binding (Figure 3A, left). These findings align with results from HDX-MS, ReX, and RMSF, which indicate that the epitope is divided into two main regions: 555-567 and 587-601, with no significant interactions starting from residue 576. To pinpoint paratope-epitope interactions we selected key binding residues based on the lowest SASA values, ensuring that consecutive residues (with at most one missing in between) were included in defining the refined paratope and epitope regions. Then we integrated SASA over these residues and compared variants with and without dynamics (Figure 3A, right). While integrating SASA over the full antibody (TZ WT and TZ variants) or full antigen (HER2) showed no distinction between binders (Figure 3, right, white), the selected residues effectively differentiated them (Figure 3, right, black). Moreover, at the key residues MD improved TZ variant ranking, making post-MD SASA more consistent with SPR affinities (Table S1).

To deepen our understanding of paratope-epitope interactions, we applied co-solvent MD Bruciaferri et al. (2024) with eight amino acid groups to probe biochemical properties across the molecular surface of unbound HER2 and TZ variants. This approach identified dominant interactions in the binding region, providing insights on enhanced surface complementarity between antibodies and their targets (Figure 3B). WT, FLJ1, FLJ2, and FLJ3 show a strong preference for negatively charged probes in the paratope complementarity to positively charged probes in the epitope. This trend is reduced in FLJ4 and FLJ5, with FLJ4 showing additional positive probe density in the paratope due to D103 in CDRH3, linked to its poor binding affinity. Both FLJ3 and FLJ4 have a unique hydrophobic patch at the binding site, with FLJ4's Y107 mutation forming hydrogen bonds with CDRL3. Increased hydrophobicity in the paratope, where the epitope shows no hydrophobic probes, may reduce binding. To summarize, we found that even a few mutations in the CDRH3 loop can disrupt the interplay between electrostatic and hydrophobic complementarity, thereby affecting antibody-antigen binding. The ranking of antibodies based on surface match aligns well with SPR data (Table S1), keeping the best binders (WT, FLJ2, and FLJ5) at the top and the worst binder (FLJ4) at the bottom in terms of paratope-epitope surface complementarity.

By focusing on the key residues identified by SASA, we found that their interatomic contacts align with SPR binding affinities (Figure 3C, top). The total interatomic contacts between paratope-epitope residues, calculated using Arpeggio Jubb et al. (2016), mirror the broader binding surface trend, suggesting these contacts alone are sufficient to reflect binding and remove the need to analyze all interface residues. After MD simulations, the number of interatomic interactions increases, but individual contact types alone do not fully capture binding differences. Analyzing multiple contact types together in an interaction graph, where nodes represent residues and edges correspond to interactions (with thicker edges indicating more interactions formed throughout MD), explains better the experimental binding affinity differences between TZ variants (Figure 3C, bottom), emphasizing the value of comparing structural properties in a refined, mechanistic manner.

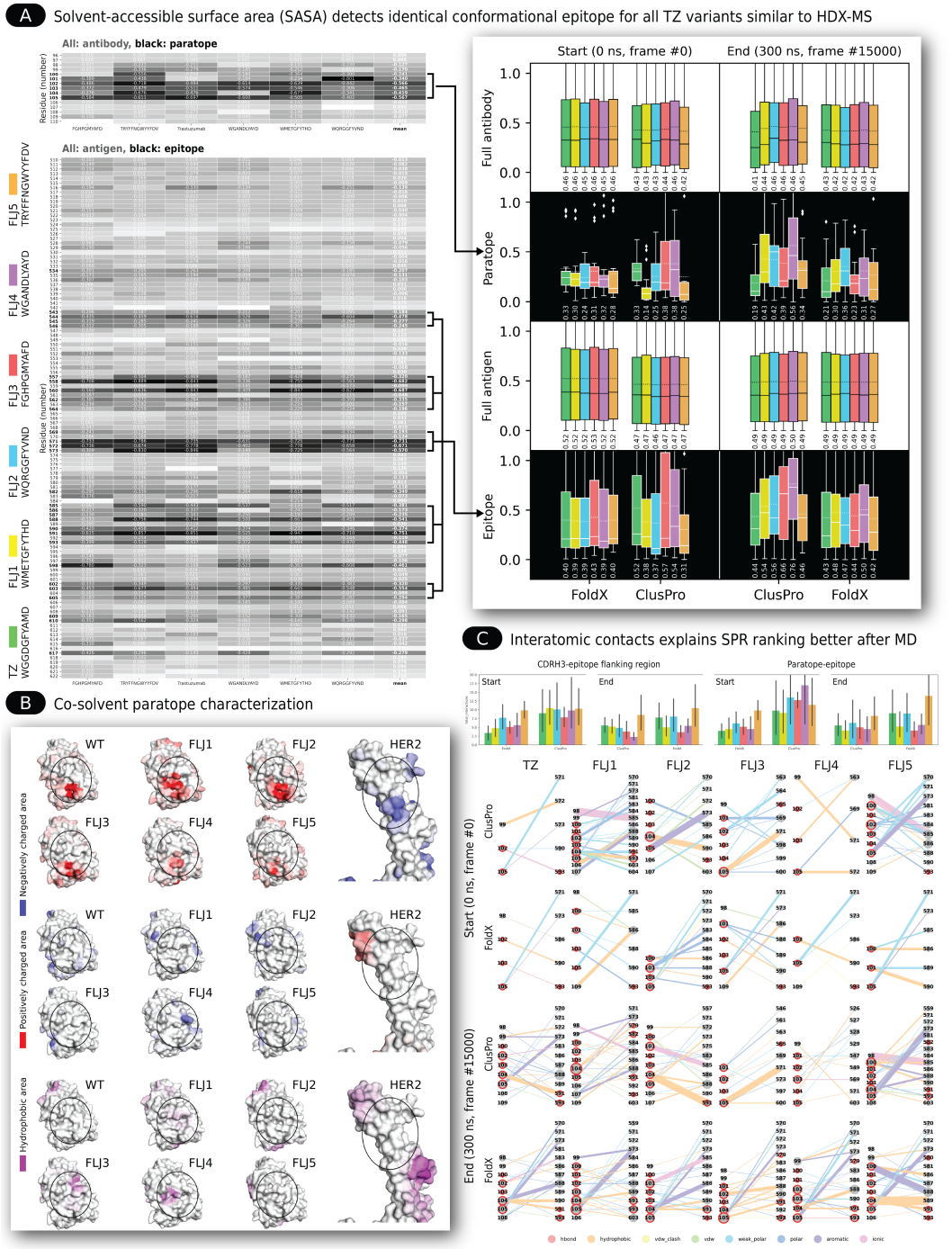

Figure 3: **TZ variants share a location-based HER2 epitope, detectable by both experimental and computational methods.** Variant colors: TZ WT (green), FLJ1 (yellow), FLJ2 (blue), FLJ3 (red), FLJ4 (purple), FLJ5 (orange). **A.** SASA analysis sharpens HDX-MS and ReX binding site definitions and distinguishes variants via paratope-epitope interactions. Normalized SASA highlights buried residues (darker), identifying key CDRH3 and epitope contacts. Selected residue SASA aligns well with SPR (black, right), especially after MD ("End"), unlike full TZ and HER2 SASA (white). **B.** Biochemical surface analysis shows complementary epitope-paratope properties. Mapping with hydrophobic (purple), positive (red), and negative (blue) probes reveals strong binders possess paratopes with opposite properties to HER2, emphasizing electrostatic and hydrophobic complementarity. **C.** Interatomic interaction analysis reveals more contacts post-MD and in strong binders. Eight interaction types are shown via barplots and networks linking paratope (left) and epitope (right). Edge thickness and color indicate interaction strength and type.

3 Conclusions

We demonstrate that conformational flexibility is crucial for extracting accurate, biochemically relevant structural features from TZ-HER2 complexes. Various computational approaches (ReX, RMSF, SASA, surface complementarity, and interatomic interactions) can identify key residues, reflecting and explaining the experimental binding affinity of TZ variants.

Our findings support a hypothesis of "sum of weak effects" in antibody-antigen binding (structural rules): to have a good binder, the candidate antibody 1) should engage in interactions with the antigen in several places throughout the epitope, 2) should not overly restrict the flexibility of the antigen, and 3) should form multiple types of weak interactions rather than few strong ones.

Taken together, we demonstrate that subtle structural shifts, detectable through accurate computational modeling and MD, are crucial for expanding our understanding of TZ variant binding to HER2.

References

Rahmad Akbar, Philippe Robert, Milena Pavlović, Jeliazko Jeliazkov, Igor Snapkow, Andrei Slabodkin, Cédric Weber, Lonneke Scheffer, Enkelejda Miho, Ingrid Haff, Dag Haug, Fridtjov Lund-Johanssen, Yana Safonova, Geir Sandve, and Victor Greiff. A compact vocabulary of paratope-epitope interactions enables predictability of antibody-antigen binding. *Cell Reports*, 34, 03 2021. doi: 10.1016/j.celrep.2021.108856.

Jonathan Barnes, Peik Lund-Andersen, Jagdish Patel, and F. Ytreberg. The effect of mutations on binding interactions between the sars-cov-2 receptor binding domain and neutralizing antibodies b38 and cb6. *Scientific Reports*, 12, 11 2022. doi: 10.1038/s41598-022-23482-5.

Habib Bashour, Eva Smorodina, Matteo Pariset, Jahn Zhong, Rahmad Akbar, Maria Chernigovskaya, Khang Lê Quý, Igor Snapkow, Puneet Rawat, Konrad Krawczyk, Geir Kjetil Sandve, Jose Gutierrez-Marcos, Daniel Nakhaee-Zadeh Gutierrez, Jan Terje Andersen, and Victor Greiff. Biophysical cartography of the native and human-engineered antibody landscapes quantifies the plasticity of antibody developability. *Communications Biology*, 7(1):922, Jul 2024. ISSN 2399-3642. doi: 10.1038/s42003-024-06561-3.

Henk Bekker, Herman Berendsen, E.J. Dijkstra, S. Achterop, Rudi Drunen, David van der Spoel, A. Sijbers, H. Keegstra, B. Reitsma, and M.K.R. Renardus. Gromacs: A parallel computer for molecular dynamics simulations. *Physics Computing*, 92:252–256, 01 1993.

Bernard Brooks, Robert Bruccoleri, Barry Olafson, David States, S. Swaminathan, and Martin Karplus. Charmm: A program for macromolecular energy, minimization, and dynamics calculations. *Journal of Computational Chemistry*, 4:187 – 217, 09 2004. doi: 10.1002/jcc.540040211.

Niccolo Bruciaferri, Eberhardt Jérôme, Manuel Llanos, Johannes Loeffler, Matthew Holcomb, Monica Fernandez-Quintero, Diogo Santos-Martins, Andrew Ward, and Stefano Forli. Cosolvkit: a versatile tool for cosolvent md preparation and analysis, 05 2024.

Qu Chen, Rajesh Menon, Lesley Calder, Pavel Tolar, and Peter Rosenthal. Cryomicroscopy reveals the structural basis for a flexible hinge motion in the immunoglobulin m pentamer. *Nature Communications*, 13, 10 2022. doi: 10.1038/s41467-022-34090-2.

Lewis Chinery, Alissa Hummer, Brij Mehta, Rahmad Akbar, Puneet Rawat, Andrei Slabodkin, Khang Quy, Fridtjof Lund-Johansen, Victor Greiff, Jeliazko Jeliazkov, and Charlotte Deane. Baselining the buzz. trastuzumab-her2 affinity, and beyond!, 03 2024.

Mark Chiu, Dennis Goulet, Alexey Teplyakov, and Gary Gilliland. Antibody structure and function: The basis for engineering therapeutics. *Antibodies*, 8:55, 12 2019. doi: 10.3390/antib8040055.

Stephen Comeau, David Gatchell, Sandor Vajda, and Carlos Camacho. Cluspro: A fully automated algorithm for protein-protein docking. *Nucleic acids research*, 32:W96–9, 08 2004. doi: 10.1093/nar/gkh354.

Oliver Crook, Nathan Gittens, Chun-wa Chung, and Charlotte Deane. Inferring residue level hydrogen deuterium exchange with rex, 04 2024.

Javier Delgado, Leandro Radusky, Damiano Cianferoni, and Luis Serrano. Foldx 5.0: Working with rna, small molecules and a new graphical interface. *Bioinformatics (Oxford, England)*, 35:4168–4169, 10 2019. doi: 10.1093/bioinformatics/btz184.

Peter Eastman, Mark Friedrichs, John Chodera, Randall Radmer, Christopher Bruns, Kyle Beauchamp, Thomas Lane, Lee-Ping Wang, Diwakar Shukla, Tony Tye, Mike Houston, Timo Stich, Christoph Klein, Michael Shirts, and Vijay Pande. Openmm 4: A reusable, extensible, hardware independent library for high performance molecular simulation. *Journal of chemical theory and computation*, 9:461–469, 01 2013. doi: 10.1021/ct300857j.

Narayanan Eswar, Ben Webb, Marc Marti-Renom, M.S. Madhusudhan, David Eramian, Min-Yi Shen, Ursula Pieper, and Andrej Sali. Comparative protein structure modeling using modeller. *Current protocols in protein science / editorial board, John E. Coligan ... [et al.]*, Chapter 2:Unit 2.9, 12 2007. doi: 10.1002/0471140864.ps0209s50.

Stian Foss, Algirdas Grevys, Kine Marita Sand, Malin Bern, Pat Blundell, Terje Michaelsen, Richard Pleass, Inger Sandlie, and Jan Andersen. Enhanced fcrn-dependent transepithelial delivery of igg by fc-engineering and polymerization. *Journal of Controlled Release*, 223, 12 2015. doi: 10.1016/j.jconrel.2015.12.033.

Dongjun Guo, Maria De Sciscio, Joseph Ng, and Franca Fraternali. Modelling the assembly and flexibility of antibody structures. *Current opinion in structural biology*, 84:102757, 12 2023. doi: 10.1016/j.sbi.2023.102757.

Yue Hao, Xinchao Yu, Yonghong Bai, Helen McBride, and Xin Huang. Cryo-em structure of her2-trastuzumab-pertuzumab complex. *PLOS ONE*, 14:e0216095, 05 2019. doi: 10.1371/journal.pone.0216095.

Damian Houde, Steven Berkowitz, and John Engen. The utility of hydrogen/deuterium exchange mass spectrometry in biopharmaceutical comparability studies. *Journal of pharmaceutical sciences*, 100:2071–86, 06 2011. doi: 10.1002/jps.22432.

Alissa Hummer, Brennan Abanades, and Charlotte Deane. Advances in computational structure-based antibody design. *Current opinion in structural biology*, 74:102379, 04 2022. doi: 10.1016/j.sbi.2022.102379.

Harry Jubb, Alicia Higueruelo, Bernardo Ochoa-Montaño, William Pitt, David Ascher, and Tom Blundell. Arpeggio: A web server for calculating and visualising interatomic interactions in protein structures. *Journal of Molecular Biology*, 429, 12 2016. doi: 10.1016/j.jmb.2016.12.004.

Gerhard Klebe. *Experimental Methods of Structure Determination*, pp. 193–214. Springer Berlin Heidelberg, Berlin, Heidelberg, 2024. ISBN 978-3-662-68998-1. doi: 10.1007/978-3-662-68998-1_13.

Andy Lau, Jürgen Claesen, Kjetil Hansen, and Argyris Politis. Deuteros 2.0: Peptide-level significance testing of data from hydrogen deuterium exchange mass spectrometry, 05 2020.

Xiaochen Lyu, Qichao Zhao, Julia Hui, Tiffany Wang, Mengyi Lin, Keying Wang, Jialing Zhang, Jiaqian Shentu, Paul Dalby, Hongyu Zhang, and Bo Liu. The global landscape of approved antibody therapies. *Antibody Therapeutics*, 5, 09 2022. doi: 10.1093/abt/tbac021.

Derek Mason, Simon Friedensohn, Cédric Weber, Christian Jordi, Bastian Wagner, Simon Meng, Roy Ehling, Lucia Bonati, Jan Dahinden, Pablo Gainza, Bruno Correia, and Sai Reddy. Optimization of therapeutic antibodies by predicting antigen specificity from antibody sequence via deep learning. *Nature Biomedical Engineering*, 5:1–13, 06 2021. doi: 10.1038/s41551-021-00699-9.

Glenn Masson, John Burke, Natalie Ahn, Ganesh Anand, Christoph Borchers, Sébastien Brier, George Bou-Assaf, John Engen, Walter Englander, Johan Faber, Rachel Garlish, Patrick Griffin, Michael Gross, Miklos Guttman, Yoshitomo Hamuro, Albert Heck, Damian Houde, Roxana Iacob, Thomas Jørgensen, and Kasper Rand. Recommendations for performing, interpreting and reporting hydrogen deuterium exchange mass spectrometry (hdx-ms) experiments. *Nature Methods*, 16:595, 06 2019. doi: 10.1038/s41592-019-0459-y.

Eliott Park and Saeed Izadi. Molecular surface descriptors to predict antibody developability: sensitivity to parameters, structure models, and conformational sampling. *mAbs*, 16: 2362788, 06 2024. doi: 10.1080/19420862.2024.2362788.

Brian Pierce, Kevin Wiehe, Howook Hwang, Bong-Hyun Kim, Thom Vreven, and Zhiping Deng. Zdock server: Interactive docking prediction of protein-protein complexes and symmetric multimers. *Bioinformatics (Oxford, England)*, 30, 02 2014. doi: 10.1093/bioinformatics/btu097.

Puneet Rawat, Divya Sharma, Ambuj Srivastava, Vani Janakiraman, and M. Gromiha. Exploring antibody repurposing for covid-19: beyond presumed roles of therapeutic antibodies. *Scientific Reports*, 11:10220, 05 2021. doi: 10.1038/s41598-021-89621-6.

Sarah Robinson, Matthew Raybould, Constantin Schneider, Wing Ki Wong, Claire Marks, and Charlotte Deane. Epitope profiling using computational structural modelling demonstrated on coronavirus-binding antibodies. *PLOS Computational Biology*, 17:e1009675, 12 2021. doi: 10.1371/journal.pcbi.1009675.

Rémi Ruedas, Rémi Vuillemot, Thibault Tubiana, Jean-Marie Winter, Laura Pieri, Ana Arteni, Camille Samson, Slavica Jonic, Magali Mathieu, and Stéphane Bressanelli. Structure and conformational variability of the her2-trastuzumab-pertuzumab complex. *Journal of Structural Biology*, 216:108095, 05 2024. doi: 10.1016/j.jsb.2024.108095.

Constantin Schneider, Andrew Buchanan, Bruck Taddese, and Charlotte Deane. Dlab—deep learning methods for structure-based virtual screening of antibodies. *Bioinformatics*, 38, 09 2021. doi: 10.1093/bioinformatics/btab660.

Arkajyoti Sengupta, Zhen Li, Lin Song, Pengfei Li, and Kenneth Merz. Parameterization of monovalent ions for the opc3, opc, tip3p-fb, and tip4p-fb water models. *Journal of chemical information and modeling*, 61, 02 2021. doi: 10.1021/acs.jcim.0c01390.

Amir Shanehsazzadeh, Sharrol Bachas, George Kasun, John Sutton, Andrea Steiger, Richard Shuai, Christa Kohnert, Alex Morehead, Amber Brown, Chelsea Chung, Breanna Luton, Nicolas Diaz, Matthew Mcpartlon, Bailey Knight, Macey Radach, Katherine Bateman, David Spencer, Jovan Cejovic, Gaelin Kopec-Belliveau, and Joshua Meier. Unlocking de novo antibody design with generative artificial intelligence, 01 2023.

Franz Waibl, Johannes Kraml, Valentin Hoerschinger, Florian Hofer, Anna Sophia Kamenik, Monica Fernández-Quintero, and Klaus Liedl. Grid inhomogeneous solvation theory for cross-solvation in rigid solvents. *The Journal of Chemical Physics*, 156, 05 2022. doi: 10.1063/5.0087549.

Ian Wilson and Robyn Stanfield. 50 years of structural immunology. *The Journal of biological chemistry*, 296:100745, 05 2021. doi: 10.1016/j.jbc.2021.100745.

Wing Ki Wong, Sarah Robinson, Alexander Bujotzek, Guy Georges, Alan Lewis, Jiye Shi, James Snowden, Bruck Taddese, and Charlotte Deane. Ab-ligity: identifying sequence-dissimilar antibodies that bind to the same epitope. *mAbs*, 13:1873478, 01 2021. doi: 10.1080/19420862.2021.1873478.

J. Word, Simon Lovell, Jane Richardson, and David Richardson. Word jm, lovell sc, richardson js, richardson dc.. asparagine and glutamine: using hydrogen atom contacts in the choice of side-chain amide orientation. j mol biol 285: 1735-1747. *Journal of molecular biology*, 285:1735–47, 02 1999. doi: 10.1006/jmbi.1998.2401.

John Xu and Mark Davis. Diversity in the cdr3 region of vh is sufficient for most antibody specificities. *Immunity*, 13:37–45, 08 2000. doi: 10.1016/S1074-7613(00)00006-6.

A Appendix

A.1 Supplementary results

We obtained FLJ1, FLJ2, and FLJ5 from the literature (Mason et al., 2021; Shanehsazzadeh et al., 2023) while FLJ3 and FLJ4 were sourced from a TZ CDRH3 combinatorial mutant library using in-house yeast display technology (similar to the one described in Chinery et al. (2024) (Methods, Table S1).

We resolved cryo-EM maps of TZ WT and all TZ variants at 4 to 7 Å resolution. Although insufficient for atomistic analysis of the binding interface, such resolution provides insights into the global structure of the complex, revealing shared HER2 binding region across all TZ variants (Figure S1). We computationally modeled TZ variants using the original TZ WT orientation ("FoldX") and two adjusted docking orientations ("ClusPro" and "zdock") and fitted them into cryo-EM maps to evaluate the model's accuracy. FoldX and ClusPro models of TZ variants and the WT fit well into the experimental cryo-EM maps, indicating that five TZ variants share similar to TZ WT HER2 binding region. For each FoldX system, we observed an average fit of 88% of atoms: TZ WT = 87% (5706 atoms out of 6530 are inside the map), FLJ1 = 93% (6115/6542), FLJ2 = 79% (5199/6540), FLJ3 = 96% (6275/6532), FLJ4 = 99% (6494/6536), FLJ5 = 74% (6551/4859). ClusPro structures show comparable to FoldX fit (TZ WT = 88% (5737/6527), FLJ1 = 93% (6077/6539), FLJ2 = 82% (5388/6537), FLJ3 = 92% (5986/6529), FLJ4 = 99% (6459/6533), FLJ5 = 77% (5068/6548), 88% of atoms inside on average), while zdock models performed the worst (TZ WT = 72% (4717/6527), FLJ1 = 77% (5056/6541), FLJ2 = 68% (4419/6539), FLJ3 = 90% (5858/6531), FLJ4 = 94% (6115/6535), FLJ5 = 68% (4426/6550), 78% of atoms inside on average).

Though FoldX models provide the best fit, ClusPro structures exhibit a comparable fit, while zdock models perform the worst. We found that the zdock starting pose significantly differs from the other two tools, and notably, orients the antibody by the framework region (not epitope) towards the antigen (Figure S1). Thus, FoldX and ClusPro were found to be reliable models, while zdock was excluded from further structural analysis, as the structural characteristics of FoldX were similar to ClusPro but differed from those of zdock.

Table S1: **Sequence and K_{on}, K_{off} and K_D description of TZ variants.** "ID" reflects the ID of each TZ variant (FLJ1-FLJ5) and the TZ WT as used in this study. "CDRH3 sequence" provides the full CDRH3 region (based on IMGT numbering scheme). "Mutations" column contains the percent of amino acid differences between the respective variant and the WT (mutations are only present in the 15-amino acid long CDRH3 region). The last three columns ("K_{on}" in 10^4/Ms, "K_{off}" in 10^{-5}/s, "K_D" in nM) summarize the binding kinetics of TZ WT and TZ variants with HER2 at pH = 7.4.

ID	CDRH3 sequence	Mutations	K_{on}	K_{off}	K_D
TZ WT	CSRWGGDGFYAMDYW	0/15 (0%)	21.5	15.5	0.72
FLJ1	CSRWMETGFYTHDYW	5/15 (33%)	5.84	6.49	1.11
FLJ2	CSRWQRGGFYVNDYW	5/15 (33%)	23.6	8.13	0.35
FLJ3	CSRFGHPGMYAFDYW	5/15 (33%)	16.3	33.3	2.03
FLJ4	CSRWGANDLYAYDYW	5/15 (33%)	7.34	564	77.5
FLJ5	CTRYFFNGWYYFDVW	10/15 (67%)	20.7	15.8	0.76

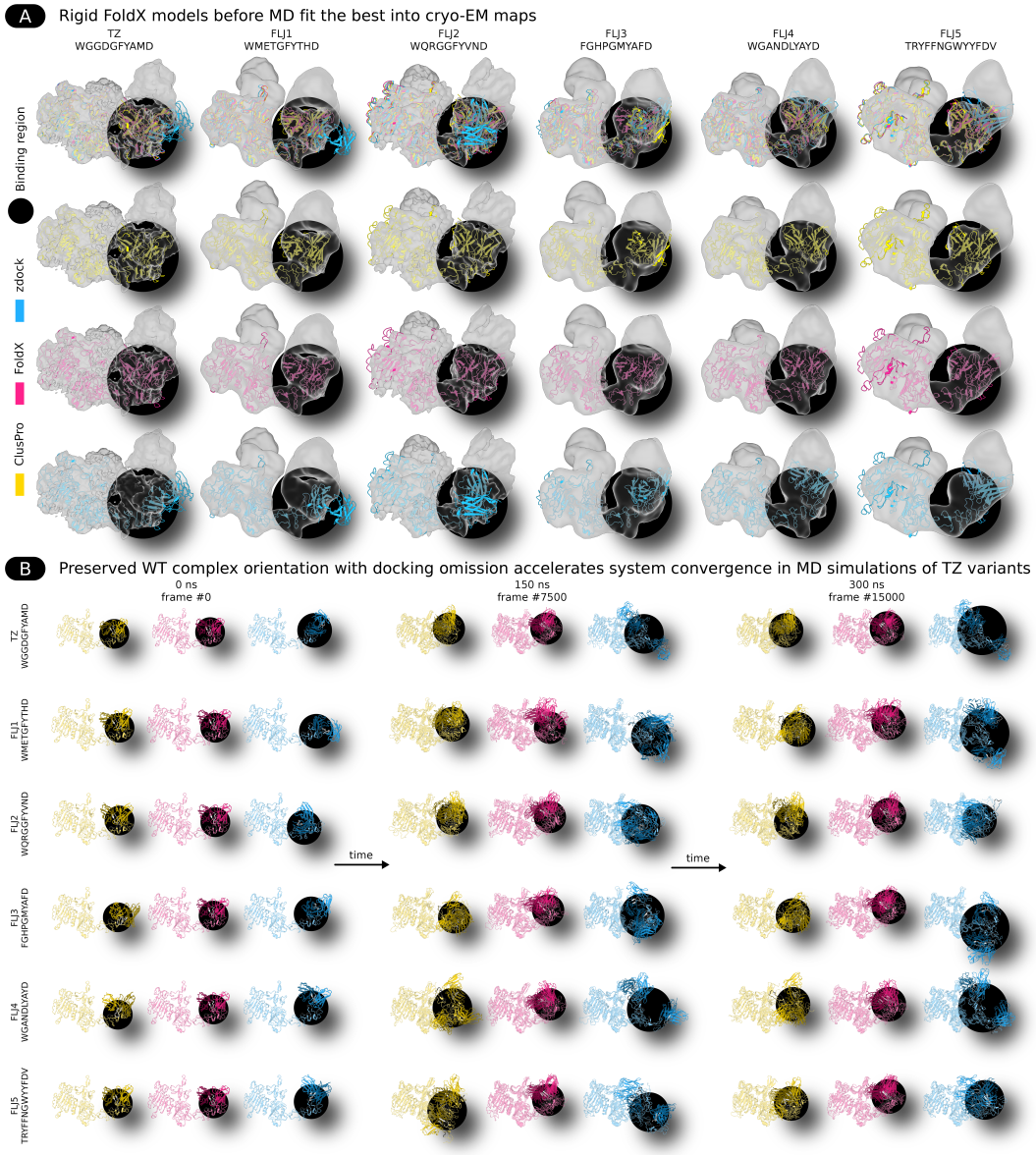

Figure S1: **FoldX and ClusPro modeled complexes fit well into the cryo-EM maps, while zdock models perform significantly worse.** Tool colors: ClusPro (yellow), FoldX (pink), zdock (blue). **A.** Cryo-EM maps show all variants bind the same region. Density maps (gray) and modeled structures (cartoons) were aligned for optimal fit. FoldX and ClusPro models have comparably successful fit, but zdock models are positioned largely outside cryo-EM maps. Binding region is shown in black. **B.** Conformational snapshots at three different stages (start, middle, end) of MD simulations. ClusPro and FoldX show minor conformational changes throughout MD, suggesting that the initial rigid conformation is close to optimal (global energy minimum). In contrast, zdock exhibits large conformational shifts even at the end of MD, indicating a suboptimal initial rigid structure that would require much longer simulation time to reach the energy minimum.

A.2 Methods

A.2.1 Proteins and antibodies

Extracellular domain region of HER2 fused with rabbit Fc was cloned in pFUSE2ss-CLIg-hK mammalian expression vector (Invivogen) and transfected by transient transfection of HEK Expi293F cells (Thermo Fisher Scientific) using manufactures' protocol. Transfection was

performed at 250 ml scale. Supernatant was collected and filtered at day 5 post transfection. Filtered supernatant was subjected to Ni^{+}-NTA affinity chromatography using His-trap column using the manufacture's protocol. Eluted HER2 was concentrated using 50 kDa spin filters (Merck) and protein was subjected to size exclusion chromatography.

WT TZ (Herceptin) was purchased from Roche. TZ variants (FLJ1-FLJ5) were synthesized as recombinant human IgG1 antibodies in HEK293 system by Sino Biological. The subsequent Fab fragments were generated from WT TZ and its variants using Fabalactica immobilized enzyme spin column kit (Genovis) following the manufacturer's protocol. Concentrations of the respective Fab solutions were determined using a NanoDrop Lite Plus Spectrophotometer (Thermo Scientific).

A.2.2 Surface plasmon resonance (SPR)

SPR experiments for determination of binding kinetics were performed using a Biacore S200 (GE Health Sciences) at 25.00 °C in (Foss et al., 2015). Polyhistidine-tagged HER2 (2 μg/ml) was immobilized on a NTA sensor chip (Cytiva) at approximately 180 resonance units (RU), according to the manufacturer's instructions. For binding experiments, phosphate-buffered saline (PBS) (8.1 mM Na2HPO4, 1.5 mM KH2PO4, 137 mM NaCl, 2.7 mM KCl) at pH 7.4 was used as running buffer and for sample dilution. Kinetics measurements were performed using 3-fold serial dilutions of Fab versions of WT TZ and TZ variants (starting between 100 and 300 nM), at a flow rate of 30 μl/min at 25.00 °C. Kinetic rate values were calculated using a simple Langmuir 1:1 ligand binding model provided by the BIAevaluation 4.1 software (Table S1).

K_{on} characterizes the antibody binding rate, K_{off} measures the rate of antibody unbinding, and K_{D} quantifies the antibody-antigen interactions at equilibrium. K_{D} can be defined using the equation:

$$K_D = \frac{K_{\text{off}}}{K_{\text{on}}} \tag{1}$$

A.2.3 Hydrogen deuterium exchange mass spectrometry (HDX-MS)

The on-exchange reaction was carried out by diluting HER2 (either in its apo-state or in complex with an antibody variant) 20-fold in exchange buffer (25 mM Tris, pD 7.1, 100 mM NaCl in D_2), resulting in a final D_2 concentration of 95%. To capture different stages of exchange, the reaction was quenched at 1, 10, 100, and 300 minutes by mixing 50 μl of the exchange reaction with an equal volume of ice-cold quench buffer (2% formic acid, 0.025% trifluoroacetic acid, 3M guanidine HCl, 0.5M Tris(2-carboxyethyl)phosphine hydrochloride), followed by flash freezing in liquid nitrogen. The quenched samples were stored at –80°C until further processing for proteolysis and liquid chromatography-mass spectrometry (LC-MS). The HDX experiment was performed in three technical replicates to ensure reproducibility.

Before analysis, the quenched samples were thawed on ice and injected into a nanoACQUITY UPLC system with HDX technology (Waters). The sample loop, UPLC, and trap columns were maintained at 0.5°C, while the pepsin column was set to 10°C. Each quenched sample (10 pmol) was injected into a 50 μl sample loop and processed in trapping mode. The protein was digested using a homemade poros pepsin column (2.1 × 30 mm, 5 μm), and the resulting peptide fragments were immediately directed to a trap column (Waters Acquity Vanguard BEH C18, 1.7 μm, 2.1 × 5 mm) for desalting. The flow rate was initially 70 μl/min for one minute, followed by 100 μl/min for an additional two minutes using buffer A (0.2% formic acid, 0.01% trifluoroacetic acid, pH 2.5). After desalting, peptides were separated using a C18 analytical column (Waters Acquity BEH C18, 1.7 μm, 1.0 × 100 mm) with a linear 5–50% acetonitrile gradient in buffer B (99.9% acetonitrile, 0.1% formic acid, 0.01% trifluoroacetic acid, pH 2.5). The gradient was applied at 40 μl/min for 17 minutes, and the eluted peptides were analyzed using a Q-TOF SYNAPT G2-Si mass spectrometer (Waters) to determine peptide identities and deuterium uptake. The mass spectrometer operated in positive ion electrospray mode with an ion mobility function, using the MSE acquisition

mode (Waters) to minimize spectral overlap. Lock mass correction with Leu-ENK peptide ensured accurate mass determination.

A.2.4 HDX-MS data evaluation

To analyze the HDX-MS data, a library of non-deuterated peptides was generated using ProteinLynx Global Server 3.0 (PLGS, Waters) with the following criteria: 1) a mass error below 10 ppm for precursor ions, 2) identification of at least two fragment ions, and 3) detection in at least two out of three non-deuterated runs. Deuterium uptake levels for peptides were quantified using DynamX 3.0 (Waters), with manual inspection to verify peptide assignments and discard noisy or overlapping spectra.

The difference in deuteration between the two states $\Delta D = [\text{HER2}] - [\text{HER2\_Antibody}]$ was calculated as a percentage by normalizing against the theoretical maximum uptake (MaxUptake), defined as $MaxUptake = N - P - 2$, where N is the number of amino acids in the peptide and P is the number of prolines. The percentage of deuteration was determined using this formula, and 95% confidence intervals for differential HDX-MS (ΔHDX) measurements at each time point were calculated using Deuteros 2.0 software Lau et al., 2020, following the approach described by Houde et al. 2011.

Confidence intervals of 95% confidence or higher for ΔHDX measurements of any individual time point were determined according to Houde et al. 2011 using the Deuteros software 2.0 Lau et al., 2020.

A.2.5 Residue-level HDX-MS (ReX)

Rex analysis was performed using the RexMS package version 0.99.7 (https://github.com/ococrook/RexMS). Default parameters were used in all cases with density set to the "laplace" option. In all cases, 5000 Markov-chain Monte Carlo (MCMC) iterations were performed for four parallel chains. Only the last 500 iterations were retained and the chain with highest likelihood over these 500 iterations was used for downstream analysis. All figures were produced as described in the RexMS tutorials (https://ococrook.github.io/RexMS/) with minor cosmetic adjustment such as choice of colours. The input data was the HDX "cluster" data for three independent experimental replicates with per peptide per time point mean imputation performed for any missing data. Charge states were combined using the mean. A peptide was discarded if it did not have a complete time-series.

A.2.6 ReX conformational signatures

ReX analysis was used to produce conformational signatures as described in the supervised conformational signature analysis with continuous outcomes as described at https://ococrook.github.io/RexMS/articles/ConformationalSignatureAnalysis.html. Again, defaults were used with the timepoints adjusted to the experimental timepoints described in the HDX experimental design. In brief, ReX builds an orthogonal partial least squares discriminant analysis (OPLS-DA) using the $-\log(K_D)$ as the outcome variable and the differential HDX data as input. The number of orthogonal and predictive components was set to one. To avoid overfitting the model was fitted using k-fold cross-validation with k set to half the input variable rounded down to the nearest integer.

A.2.7 Cryogenic electron microscopy (cryo-EM)

Pertezumab, WT TZ, and TZ variants were digested into Fab and Fc using 1% w/w activated papain for 5 hours at 37°C. CaptureSelect IgG-Fc (multispecies) affinity matrix was added to digested antibodies to bind undigested IgG and Fc. The remaining Fab was purified through size exclusion chromatography with a GE S200i column. HER2 was incubated with a combination of TZ variant Fab or IgG and Pertezumab Fab or IgG overnight at 4°C. Cryo-EM grids were frozen on a Vitrobot IV (Thermo Scientific) with UltraAuFoil 1.2/1.3 Au 300, Quantifoil 1.2/1.3 Cu 300, or 1.2/1.3 Au 400 graphene oxide grids using 0.01 mM LMNG mixed in immediately before loading onto the grid. Complexes were collected on a

Glacios 1 equipped with a Falcon 4 CCD or a Glacios 2 equipped with a Falcon 4i CCD. Micrographs were collected using EPU and initially processed in Cryopsparc Live. 3D maps were generated in Cryosparc using non-uniform refinement.

A.2.8 Preprocessing of structures

We utilized the Cryo-EM structure of the WT HER2-trastuzumab complex (PDB ID: 6OGE) for in silico analysis, given its resolved binding interface and reliable resolution of 4.36 Å Hao et al., 2019. The structure was further cleaned in PyMOL by removing the heteroatoms, pertuzumab Fab chains and constant regions in TZ chains. The missing residues (residue 127-129) in HER2 chain were modeled using MODELLER Eswar et al., 2007 and hydrogen atoms were added using Reduce Word et al., 1999. For consistency, we have used chain H, L and A for heavy chain, light chain and antigen (HER2) chain, respectively. The HER2 chain was extracted from the complex to be used as antigen for docking.

A.2.9 Computational mutagenesis

The same 6OGE structure was used as a starting point for molecular modeling. We mutated the WT TZ-HER2 complex using FoldX 5.0 Delgado et al., 2019 to generate the variant complex structures Barnes et al., 2022. The PDB file was first corrected using the "RepairPDB" command and mutant structures were generated using "BuildModel" command. In addition, we also calculated the interaction energies of the new HER2-trastuzumab variant complexes using the "AnalyseComplex" command. The change in interaction energy upon point mutation was calculated using following formula:

$$\Delta\Delta G_{\text{mutant}} = \Delta G_{\text{mutant}} - \Delta G_{\text{WT}} \tag{2}$$

A.2.10 Computational mutagenesis

Due to imperfections of computational models and unknown binding interface of the mutated TZ variants, we decided to apply several docking tools after the FoldX mutagenesis to test the antibody-antigen orientation from different perspectives and verify the limitations of each individual tool. Out of all available docking tools we selected two specific docking methods due to their distinct (yet similar) algorithmic approaches and they previously showed reasonable results in antibody-antigen tasks (referred to as "ClusPro" or "zdock" respectively). The first docking tool, zdock 3.0.2 Pierce et al., 2014, is a Fast Fourier Transform (FFT) based protein docking program, which utilizes an empirical energy-based scoring function to evaluate each pose. The second docking tool, ClusPro 2.0 Comeau et al., 2004, is also based on FFT and energy scoring function, however, selected poses are further processed by identification of few low energy clusters and energy minimization of the cluster centers with CHARMM Brooks et al., 2004. The binding interface for the WT complex was delineated by considering a contact distance of 4.5 Å between heavy atoms. These identified residue positions were further utilized in information-driven docking as potential binding regions. In ZDOCK 3.0.2, we specified both paratope and epitope residues for docking and generated 20 docked structures. Similarly, the docked structures were generated using antibody mode in ClusPro 2.0 online server, where only epitope residues were provided for docking in "attraction and repulsion section" and "mask non-CDR regions" was kept true to avoid docking to non-CDR regions. The top docked structures obtained from the ZDOCK 3.0.2 and ClusPro 2.0 were further analyzed to determine the best docking pose. We calculated the interaction energies for all docked structures using FoldX 5.0 and fnat score Schneider et al., 2021 as described previously Rawat et al., 2021. In summary, The docked structure with highest fnat score was selected as the final docked structure. However, if there were multiple structure with the same fnat score, then the structure with best interaction energy was selected as the final docked structure. The final complex structure for each TZ variant was selected from the docked structures generated by each method based on two filtering criteria: 1) fnat score (see Methods for more detail) and 2) interaction energies calculated using FoldX 5.0, if necessary. All 3 types of the final variant complexes ("FoldX", "ClusPro", "zdock") fit into the cryo-EM density maps with ChimeraX.

A.2.11 Molecular dynamics (MD)

Hydrogens were added to initial antibody structures using Reduce Word et al., 1999. All MD steps were performed in GROMACS v.2022.4 Bekker et al., 1993. We used AMBER99SB-ILDN force field and TIP3P water model for MD system preparation. The simulation box was defined as a cube centered around the antibody placed at the 2 nm distance between the solute and the box. All systems contained both Na and Cl ions at 0.1 mol/liter salt concentration. We minimized the energy of each initial system with the steepest descent algorithm for 20000 steps. For the equilibration, we first considered constant volume simulations (NVT) at 300 K for 100 ps and followed up by constant pressure simulations (NPT) at 1 bar for another 10 ns. During these equilibration simulations (NVT and NPT), where applicable, we used the Parrinello-Rahman barostat and V-rescale thermostat with velocity rescaling using 0.1 ps and 0.1 ps time constants, respectively. During all the simulations, we constrained the length of all bonds using the linear constraint solver (LINCS) algorithm and kept the water molecules rigid via the SETTLE algorithm. We used particle mesh Ewald (PME) for treating the electrostatic interactions with a real-space cutoff of 1.0 nm. We simulated 3 repetitions of 300 ns independent production runs with 2 fs time step for each system, all continued from the last step of the NPT simulations at 300 K and 1 bar using a 2 fs time step.

A.2.12 Postprocessing of MD simulations

MD trajectories were processed using GROMACS Bekker et al., 1993. Systems were centered inside the simulation box. We disabled the use of periodic boundary conditions (PBC) during frames extraction and prevented atoms from jumping across the box boundaries. It made all molecules (both antibody and antigen) "whole" through the simulations. We skipped every 100th frame during the trajectory conversion and saved the remaining protonated protein conformations in separate PDB files. We applied the same approach to all systems.

A.2.13 MD convergence calculations

We used MDAnalysis to calculate RMSD-based convergence of each trajectory. The distance was calculated in Aangstrom between each conformation through the 300 ns (15000 frames) MD simulation and its first frame. We analyzed the distances obtained in comparison of both antibody and antibody-antigen backbones. All MD simulations converged starting from 100 ns based on the visual analysis of the convergence plots. The ab-ag convergence exhibits higher fluctuations but ultimately converges similarly to only the ab one. Hence for the data analysis we decided to use 100 ns (frame 5000) onwards. RMSD values for all runs and systems were averaged across 3 runs and plotted with seaborn.

A.2.14 Co-solvent paratope characterization

To characterize the effect of mutations on the paratope, we applied the recently developed CosolvKit Bruciaferri et al., 2024 using a predefined minimal set of fragments designed to mimic the key features of standard amino acid side chains. This set includes hydrophobic, hydrogen bond donors, hydrogen bond acceptors, aromatic, positively charged, and negatively charged probes. The starting structures for the simulations were prepared and protonated in MOE (Molecular Operating Environment). We soaked the protein into a cubic water box, using TIP3P-FB water molecules Sengupta et al., 2021, applying a wall distance of 12 Å around each structure and including a mixture of amino acid-mimicking probes, set to a concentration of 0.1 M each. Sufficient NaCl was added to neutralize the systems Eastman et al., 2013. Each investigated Fv variant was simulated for 200 ns using OpenMM Eastman et al., 2013. All other simulation parameters were set according to standard protocols Bruciaferri et al., 2024. For the analysis of the simulations, the CosolvKit post-processing pipeline was used to generate density maps for each individual probe. The resulting density was then localized onto the protein surface using gisttools Waibl et al., 2022.

A.2.15 Root mean squared fluctuations (RMSF)

RMSF measures the flexibility of atoms or residues in MD simulations. We used MDanalysis to compute RMSF for all MD trajectories. The data was plotted with seaborn.

A.2.16 Solvent-accessible surface area (SASA)

SASA was calculated separately for bound and unbound complexes of HER2 and TZ WT and TZ variants. We subtracted the unbound SASA values from the bound values to investigate only the binding-caused differences in contacts. The data was plotted with seaborn.

A.2.17 Interatomic contacts

Processed frames in PDB format were converted into CIF using the MAXIT program. Then, we used pdbe-arpeggio Jubb et al. (2016) to extract all the interatomic interactions. Next we applied custom Python scripts to get the only selected contacts (key residues) and the parts of the structure we are interested in (antibody, antigen, paratope, epitope). The choice of the parameters were made based on general biochemical understanding of antibody-antigen interactions and their use for orthogonal antibody-antigen design (nonredundant normally distributed interactions that have low pairwise correlation).

A.3 Data availability

Experimental and computational data, along with related scripts and pipelines, will be released upon formal publication through Zenodo, GitHub, and similar platforms.